Experimental confirmation of Zener-polaron-type charge and orbital ordering in $Pr_{1-x}Ca_xMnO_3$

L. Wu,[1] R. F. Klie,[1,2] Y. Zhu,[1,*] and Ch. Jooss[3,†]

[1]*Department of Condensed Matter Physics and Materials Science, Brookhaven National Laboratory, Upton, New York 11973, USA*

[2]*Department of Physics, University of Illinois at Chicago, Chicago, Illinois 60607, USA*

[3]*Institute of Materials Physics, University of Goettingen, Friedrich-Hund-Platz 1, 37077 Goettingen, Germany*

(Received 3 May 2007; revised manuscript received 2 July 2007; published 30 November 2007)

$Pr_{1-x}Ca_xMnO_3$ in the doping range between $0.3<x<0.5$ represent an extremely interesting manganite system for the study of the interplay of different kinds of ordering (charge, orbital, lattice, and spin). While there is consensus that a charge- and orbital-ordered state develops below a transition temperature $T_{co} \approx 230$ K, recent controversial structural refinements resulting from neutron and x-ray diffraction studies challenged our understanding of the particular type of charge ordering (CO) and orbital ordering (OO), and consequently, the underlying mechanism of the colossal resistance effects. Here, we present a detailed high-resolution transmission electron microscopy and electron-diffraction study that, based on extinction rules, resolves the current controversy and confirms the existence of the Zener-polaron (ZP)-type CO and/or OO in $Pr_{1-x}Ca_xMnO_3$. The ZP-type ordering is further verified by atomic-column-resolved electron energy-loss spectroscopy revealing strong charge ordering of the in-plane oxygen-Mn bonds, while valence disproportionation at the Mn sites is less than expected. Over wide doping and temperature ranges, we observed structural phase coexistence between the ZP-CO/OO $P2_1nm$ and the disordered $Pbnm$ structure.

DOI: 10.1103/PhysRevB.76.174210 PACS number(s): 71.27.+a, 61.14.Lj, 68.37.Lp, 79.20.Uv

I. INTRODUCTION

Perovskite manganites ABO_3 (B=Mn) represent an especially illuminating example of materials with strongly correlated electrons, wherein the interplay of four degrees of freedom, lattice, orbital, charge, and spin, generates a complex variety of ground states, including different types of orbital, charge, and spin orderings.[1–4] An important aspect is that no single interaction or degree of freedom dominates in these materials. Consequently, subtle changes of external and internal parameters such as temperature, external electric or magnetic fields, strain, ionic radii, quenched disorder, and even sample history may tremendously affect the organization of the correlated electron and lattice system into different ground states. Fascinating transport properties, such as colossal resistance effects, are related to such field-induced phase transitions between different ground states and types of ordering.

The structure and electronic properties of manganites strongly depend on the ionic radius of the rare earth ion.[5] The tolerance factor, $t=d_{A,O}/\sqrt{2}d_{B,O,}$ compares the oxygen bonding lengths, $d_{A,O}$ and $d_{B,O,}$, of the A and B site ions in a cubic structure, respectively, based on the ionic radii. For $t<1$, the resulting compressive strain on the B-O-B bonds is relaxed by octahedral tilting,[6] which strongly influences the electronic bandwidth of relevant conduction bands[7] and may modify energy scales and symmetries of the Jahn-Teller (JT) distortion.[6] The presence of JT active Mn^{3+} cations greatly enriches the possible types of structural distortions of the ideal cubic parent compounds. Their occurrence affords an additional ligand-type interaction between the static- or dynamic-structural distortion of the MnO_6 octahedra and the bonding state of the e_g-conduction electrons, and lifts the double degeneracy of the e_g states. In addition to the first-order JT effect that retains the center of symmetry, a second-order JT distortion[8] may develop, breaking the centrosymmetry by the off-center movement of the transition-metal ion; in turn, this may influence the localization mechanism of the electrons in different types of charge-ordered (CO) and orbital-ordered (OO) states. The material system $Pr_{1-x}Ca_xMnO_3$ is particularly interesting: The Pr^{3+} and Ca^{2+} ions are small ($t \approx 0.94$) and have approximately the same size of 1.18 Å, and consequently, structural distortions due to different degrees of cation disorder are expected to be negligible. Depending on the Ca concentration, the system exhibits a series of semiconducting and insulating phases with different types of orbital, magnetic, and charge orders.[9–11] The electronic bandwidth of the e_g electrons is very narrow, and the related insulating ground states can be transformed into conducting ferromagnetically ordered states only by applying external forces. The changes in resistivity during the insulator-metal transition in external magnetic fields of the $Pr_{1-x}Ca_xMnO_3$ ($0.3<x<0.5$) compound is 10 orders of magnitude,[12–14] among the highest ever observed. In addition to this colossal magnetoresistance effect, colossal resistance effects may be induced electrically,[14,15] via photon exposure[16] and by strain.[17] The CO and/or OO transition at $T_{co} \approx 230$ K is well separated from the magnetic ordering transition of the charge-exchange-type (CE) antiferromagnetic phase at $T_N \approx 130$ K.[17]

The structure of the high-temperature paramagnetic insulating phase ($T \gg T_{co}$) is well established in the full doping regime. Strong tilt distortion of the MnO_6 octahedra with tilt angles around 15° is associated with an orthorhombic $Pbnm$ unit cell (space group No. 62).[9] It has four equivalent MnO_6 octahedra, which are related by the 1, 2_1, n, and m symmetry operations. Due to the presence of a strong JT interaction for the Mn^{3+} cations, transport behavior is well characterized by the thermally activated motion of small JT polarons.[14,18] A decrease in temperature increases correlated polaron behavior, which may be a driving force for the long-range orbital and charge ordering at T_{co}. In contrast to the high-temp-

erature phase, there is controversial experimental data on the atomic and electronic structures of the CO and/or OO phase below T_{co}. In the conventional checkerboard-type (CB) CO and/or OO picture, originally introduced by Goodenough in the 1950s,[19] the CO is believed to consist of a CB-type pattern of Mn^{3+} and Mn^{4+} ions, where the Mn^{3+} sites are JT distorted while Mn^{4+} sites are not. In this picture, e_g-electron localization is due to occupancy of the Mn^{3+} sites, and their orbitals orientationally align in a cooperative manner in the *a-b* plane. Below T_N, magnetic long-range ordering forms a CE-type antiferromagnetic state with ferromagnetically coupled zigzag chains. However, a recent neutron scattering study by Daoud-Aladine *et al.*[20] found a Zener polaron (ZP) ordered state in $Pr_{0.6}Ca_{0.4}MnO_3$, while resonant x-ray diffraction[21] (RXD) and x-ray-absorption near-edge structure (XANES) studies[22] revealed that the charge disproportionation, δ, between the different Mn sites in the superstructure is $\delta \ll 1e$. Thus, in contrast to the findings of Daoud-Aladine *et al.*, RXD[21] supports the CB structure for $Pr_{0.6}Ca_{0.4}MnO_3$. Furthermore, a recent high-resolution x-ray and neutron diffraction study for the samples with $x=0.5$ (Ref. 23) obtained slightly better refinements for the CB structure than for the ZP one.

Although theoretical work has contributed to our understanding of the electronic configuration of both controversial structures, it has not clearly favored either one. On the one hand, it was shown that a CB-type CO and/or OO state with $\delta \ll 1e$ can exist in half-doped manganites,[24] such that two unequivalent $Mn^{3.5+}$ sites with a small or zero charge disproportionation can have two different orbital configurations. Other *ab initio*[25] and unrestricted Hartree-Fock calculations[26] predict that the ZP-ordered state may be favorable under certain conditions in half-doped manganites, and a recent theoretical paper[27] shows that lowest energy ZP- and CB-type ordered states may differ only by slight displacements in the positions of key oxygen and Mn atoms. Efremov *et al.*[28] discussed both types of structures with respect to site-centered charge ordering at Mn sites or bond-centered charge ordering at Mn-O-Mn dimers, forming the ZP-ordered state. Furthermore, they considered a mixed configuration that might form a different type of ferroelectric ordering.

The general challenge in accurately determining the space group and refinement of the structure in the ordered state is the heavy twinning present in all PrCaMnO single crystals, ceramic powders, and films on length scales of 10–100 nm. The presence of six twin variants in the disordered state with *Pbnm* symmetry and pseudocubic lattice constants $a/\sqrt{2} \approx b/\sqrt{2} \approx c/2$ may lead to overlapping of the superstructure and Bragg diffraction peaks in the ordered state, thereby complicating the structural refinements involving volume-averaged macroscopic diffraction measurements. Consequently, resolving the present controversy requires the use of local probes.

In this paper, we report our extensive transmission electron microscopy (TEM) study of $Pr_{1-x}Ca_xMnO_3$ polycrystalline bulk material and epitaxial thin films with one-third and one-half dopings ($x=0.32$ and $x=0.50$). By combining electron diffraction, high-resolution TEM (HRTEM), atomic-resolution scanning TEM (STEM), and electron energy-loss spectroscopy (EELS), we shed light on the controversies and confirm the presence of ZP-type ordering. Although the use of incident electrons for structure refinements, due to multiple scattering, is more complicated than neutrons or photons, the analysis of individual twin and ordered domains, together with the application of extinction rules for various Bragg reflections, allows us to place strong constraints on the possible superstructure models. Our detailed analysis of the $2b_0$ superstructure gives strong evidence for a Zener polaron-like charge and orbital ordered (ZP-CO/OO) state, wherein the e_g electrons are ordered on the oxygen site of ordered Mn-O-Mn bipolarons while maintaining a very small degree of valence disproportionation, $\delta \ll 1e$, on the Mn sites. Using bond-valence-sum analysis and angular dependence of the hopping probability in Mn-O-Mn orbitals, Mn valence states, the degree of orbital polarization, and a qualitative picture of the distribution of the e_g electrons in the *p-d*-hybrid orbitals are obtained.

II. EXPERIMENTAL AND THEORETICAL METHODS

Polycrystalline samples of $Pr_{1-x}Ca_xMnO_3$ (PCMO) with $x=0.32$ and $x=0.50$ and grain sizes of about 1 μm were prepared by repeated grinding, pressing, and heating of a stoichiometric mixture of high purity (99.99%) $CaCO_3$, Mn_2O_3, and Pr_6O_{11} powders. The powders were heated prior to mixing for dehydration, and the stoichiometric mixture was prepared under an argon atmosphere. Each sample was heated at 1050 °C for 24 h and grinded afterwards; the full procedure was repeated three times. The solid-state reaction and the lattice parameters after pure-phase formation were controlled by x-ray diffraction in Bragg-Brentano geometry. After the reaction was completed, the pure-phase powder was pressed and sintered to pellets. X-ray diffraction, electron diffraction, energy dispersive x-ray spectroscopy, and *Z*-contrast (*Z* refers to atomic number) imaging in STEM as well as EELS revealed single-phase samples without any variation of the stoichiometry within the limits (~2%) of the experimental measurements. PCMO thin films were grown on single-crystalline $SrTiO_3$ (001) substrates by pulsed laser deposition. Details of the film growth were reported elsewhere.[14] Electron-transparent samples were first carefully cut using a low-speed wire saw. The specimens then were mechanically polished, dimpled to about 50 μm at the center, and ion milled to perforation at low temperature (−60 °C) to minimize sample damage.

The main results presented in this paper were obtained using the JEOL3000F TEM/STEM, equipped with an ultrahigh-resolution objective-lens pole piece, an off-axis 1024×1024 Gatan slow-scan camera, a Fischione annular dark-field (ADF) detector, a postcolumn Gatan imaging filter, and a NORAN x-ray detector. The instrument can be operated in either TEM or STEM mode. The single-domain electron diffraction was obtained either by selected-area electron diffraction (SAED) that can select a small area with a diameter of ~120 nm, or by nanodiffraction with a beam of a few nanometers. Simulations of the high-resolution image and electron diffraction were obtained by the many-beam Bloch-wave method.[29] Valence-sum analyses were performed using the method of Brown and Altermatt.[30] To

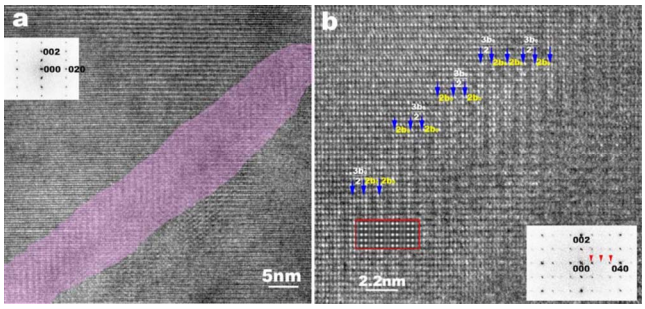

FIG. 1. (Color online) (a) Low magnification image of phase separation between the C and/or O disordered phase and the CO and/or OO (pink shaded) phase of $Pr_{0.5}Ca_{0.5}MnO_3$. The inset is the FFT from the disordered area (top-left area). (b) Magnified high-resolution image from the shaded area in (a). The arrows indicate the ordering along the b direction. We note that there are two kinds of ordering: one is $2b_0$ and the other is $\frac{1}{2}$ $(3b_0)$. The inset of (b) is the FFT of the image. The positions of the superlattices in the FFT deviate from the rational positions indicated by the arrows, which are caused by the mixture of $2b_0$ and $3b_0$ superstructures. The embedded image of the boxed area is the simulated HRTEM based on our ZP model listed in Table I. It is in good agreement with the experiment.

roughly estimate the differences in orbital occupation as function of local variation of Mn-O-Mn bonding angles,[31] a linear relation between occupation and bonding angles was assumed in the angular regime between 152° and 165°, where a large difference in ferromagnetic exchange, from zero to its maximum, occurs in manganites.[32]

III. EXPERIMENTAL RESULTS

A. High-resolution transmission electron microscopy and electron diffraction

The inspection of several bulk samples with $x=0.32$ and $x=0.50$ by SAED and HRTEM at room temperature (RT, ~300 K) revealed the presence of structural- and electronic-phase separations between the charge and/or orbital (C and/or O) disordered state and the CO and/or OO state. A typical observation is presented in Fig. 1(a), where the electron beam is along the [100] direction. The top-left and bottom-right area are C and/or O disordered phases with lattice constant $b_0=0.5403$ nm, while in the middle (pink area) there is a CO and/or OO phase with mixed $2b_0$ (unit-cell doubles along the b direction) and $3b_0$ (unit-cell triples along the b direction) superstructures. Figure 1(b) is the magnified image from Fig. 1(a). The arrows indicate the $2b_0$ superstructure unit cell and half of a $3b_0$ superstructure unit cell. The fast Fourier transform (FFT) image of the superstructure is shown in the inset of Fig. 1(b). A careful inspection indicates that the superlattice spots, e.g., 010 and 030, are actually not at the rational positions, which apparently is due to the mixed $2b_0$ and $3b_0$ superstructures rather than to a single incommensurate ordering along the b direction. Overall observations show that all samples (1/3 and 1/2 dopings) are dominated by the C and/or O disordered $Pbnm$ phase with a small amount of ordered phases at room temperature. The size of ordered domains ranges from 10 to 100 nm, and all ordering occur along the b direction. In addition to the $2b_0$ and $3b_0$ superstructures, we found $5b_0$ superstructures (unit-cell quintupled along the b direction). These three kinds of superstructures may exist individually, or coexist in the same domain. Quantitative information about the volume fraction of the ordering phases is difficult to acquire since the field of view in HRTEM is small and the visibility of the superlattice fringes and diffraction spots depends on the crystallographic orientation. Roughly speaking, the ratio of the ordered over the disordered phase at RT is of the order of 10%. We emphasize that all types of CO and/or OO domains are already visible at room temperature, which is above the nominal ordering temperature of $T_{co}\approx 230$ K. By cooling the samples down to 80 K, the volume of the $2b_0$ ordered phase markedly increases, while the volume of $3b_0$ and $5b_0$ ordered phases is almost unchanged. In fact, at 80 K, the samples ($x=0.32$ and $x=0.50$) were dominated by the $2b_0$ ordered phase. Here, we focus only on understanding the properties of the type of CO and/or OO state with doubled unit cell along the b direction. Not only is this the dominant superstructure, but it also exhibits the most pronounced temperature dependence. Thus, the $2b_0$ superstructure modulation is most strongly related to the phase transition from a C and/or O disordered state to a CO and/or OO state observed by macroscopic measurements.

The presence of six twin domains with very small twin sizes may lead to the misinterpretation of Bragg reflections in the volume-averaged macroscopic diffraction measurements due to mixing of diffraction spots from different domains. Although SAED and nanodiffraction are considered to be more difficult in refining crystal structures compared to the high-resolution neutron or x-ray diffraction due to the multiscattering effects, its advantage in probing small areas, such as individual domains, could provide exclusive structural information. To circumvent the multiscattering problem, we examine the superlattice intensity distribution at thin areas and/or tilt the domain off zone axis to minimize its effects. Figures 2(a)–2(c) show the SAED patterns of the ordered phase within an *individual* twin domain for the three main zones, [001], [010], and [100]. In addition, Fig. 2(e) gives an example of the resulting diffraction pattern when two domains were selected in SAED. Based on these diffraction patterns, we derived the general reflection conditions for the $2b_0$ ordered phase as follows: allowed reflections without conditions for hkl, $hk0$, $0kl$, and $0k0$; and those with condition for $h0l$: $h+l=2n$: $h00$: $h=2n$, and $00l$: $l=2n$. These reflection conditions are observed in all $2b_0$ ordered phases regardless of the composition and temperature. This rules out the space groups $P112_1/m$ and $P11m$, which are usually applied for the CB-type CO and/or OO state. Only $P2_1nm$ is consistent with the above general reflection conditions. Moreover, for $0kl$ reflections, the reflections with $k/2=2n+1$ are all invisible, which is exclusively observed only when a single domain with its [100] direction parallel to the beam is probed [Fig. 2(c)]. These invisible reflections show up when the other domain, with its [010] direction parallel to the beam, is chosen. In Fig. 2(e), the weak spots at 021, 023, etc., are actually due to the contribution of the 101, 103, etc., reflections from the [010] domain. The additional extinction

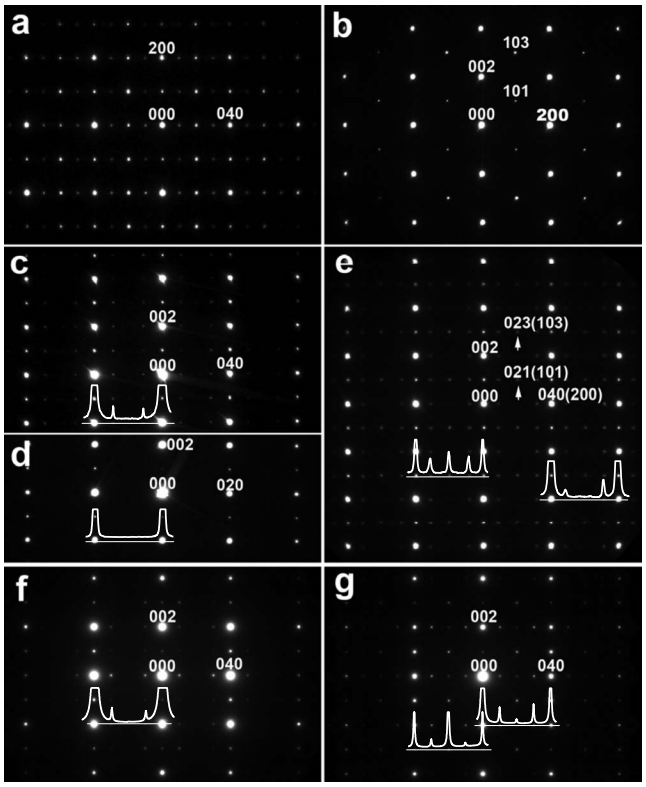

FIG. 2. (a)–(c) Selected-area electron-diffraction patterns of the ordered phase of $Pr_{0.5}Ca_{0.5}MnO_3$ along the [001], [010], and [100] directions, respectively. (d) The [100] diffraction of the disordered phase for comparison with (c). (e) The diffraction pattern containing both the [100] and [010] domains. Note that the spots at the position indicated by the arrows in (e) are invisible in (c) and (d). The weak spots, e.g., 101, 103, etc., come from the [010] domain (indexed in parentheses). (f) Simulated electron-diffraction pattern based on our Zener polaron model showing good agreement with the experimental pattern in (c). (g) Simulated electron-diffraction pattern based on the model of Daoud-Aladine *et al.* that does not agree with the single-domain experimental observations. For clarity, intensity profiles of line scans across Bragg and superlattice reflections (marked as white lines) are also included in (c)–(g).

for the $2b_0$ superstructure is important in refining the structure of the ordered phase, which we will discuss later. By including both ordered and disordered domains in the selected area aperture, we obtained the diffraction patterns with both ordered and disordered phases, which can be used to accurately determine the lattice difference between the ordered and disordered structures. We found that the ordered lattice is slightly shrunk along the b direction compared to the disordered one with $b_s/2b_0=0.983$, where b_s and b_0 are the lattice parameters b of the ordered and disordered phases, respectively. This indicates a change in the specific volume between the C and/or O ordered and disordered phases. Clearly, the phase transition between both structures is the first-order one.

B. *Z*-contrast scanning transmission electron microscopy

Before addressing details of the derived structure model from the diffraction patterns, we consider the rule of the Pr/Ca and MnO_6 sublattices in generating the superlattice modulation. A thin ordered area with its [100] direction parallel to the beam was selected first in the TEM mode, then switched to the STEM mode to acquire a series of atomic-resolution ADF images.[33–36] The key to atomic-resolution ADF imaging[37–39] is the formation of the smallest possible electron probe (~0.13 nm) with sufficient probe current (40 pA) to obtain statistically significant images and spectra.

The experimental setup of the microscope allows the low-angle-scattered electrons, which do not contribute to the ADF image, to be used for EELS.[40] As the two techniques do not interfere, this means that the ADF images can be used to position the electron probe at the desired spot on the sample while acquiring spectra[41,42] (see Sec. III D). The lens conditions in the microscope and spectrometer were set up for the smallest probe size, with a convergence semiangle α of 11 mrad, while the detector inner angle was varied from 120 to 15 mrad to allow us to change the amount of phase information in the ADF image (*Z*-contrast or high-angle annular dark field images require that the collection angle is larger than 30 mrad for $\alpha=11$ mrad; for collection angles smaller than 30 mrad, medium-angle annular dark field (MAADF) images are recorded). To guarantee the highest spatial resolution and avoid thermal drifting, all investigations were performed at RT.

Figures 3(a) and 3(b) show two ADF images with the largest and smallest detector inner angles (i.e., high-angle and medium-angle annular dark field images). In both images, the image intensity is proportional to the average atomic number (Z) per column. Therefore, the bright spots correspond to atoms with the highest Z value, i.e., Pr and Ca. By visual inspection of the images, no superlattice can be determined, in contrast to the HRTEM observation of the same area. Fourier transformation of both STEM images, however, reveals very weak superlattice spots, whose intensity is slightly enhanced as the collection angle is reduced. By reducing the collection angle, i.e., increasing the phase contribution to the image, the ADF image becomes increasingly more sensitive to the bonding conditions of the material. This means that the observed superlattice peaks are not due to cation ordering on the A site, since this effect would have resulted in an increased intensity of superlattice spots with increasing detector angle. Figure 3(c) shows a slightly low-pass filtered STEM image of an ordered area with a doubled unit cell. The related line scan of the Pr/Ca columns in Fig. 3(d) shows only stochastic modulations, but no indication of cation ordering. The same set of experiments was repeated for other sample areas and for the $b_s=5b_0$ superstructure. In none of the experiments did we observe a superlattice due to A-site cation ordering, in full agreement with macroscopic diffraction data, where refinement does not reveal any cation ordering. These results are in contrast to recently observed A-site ordering in $La_{0.75}Ca_{0.25}MnO_3$ films that exhibit a rhombohedral lattice while having an orthorhombic structure in the A-site disordered state.[44] Our ADF imaging results provide additional proof that the origin of the structural and electronic modulations in $Pr_{1-x}Ca_xMnO_3$ are due to a modulation of the MnO_6 octahedra, rather than to A-site order.

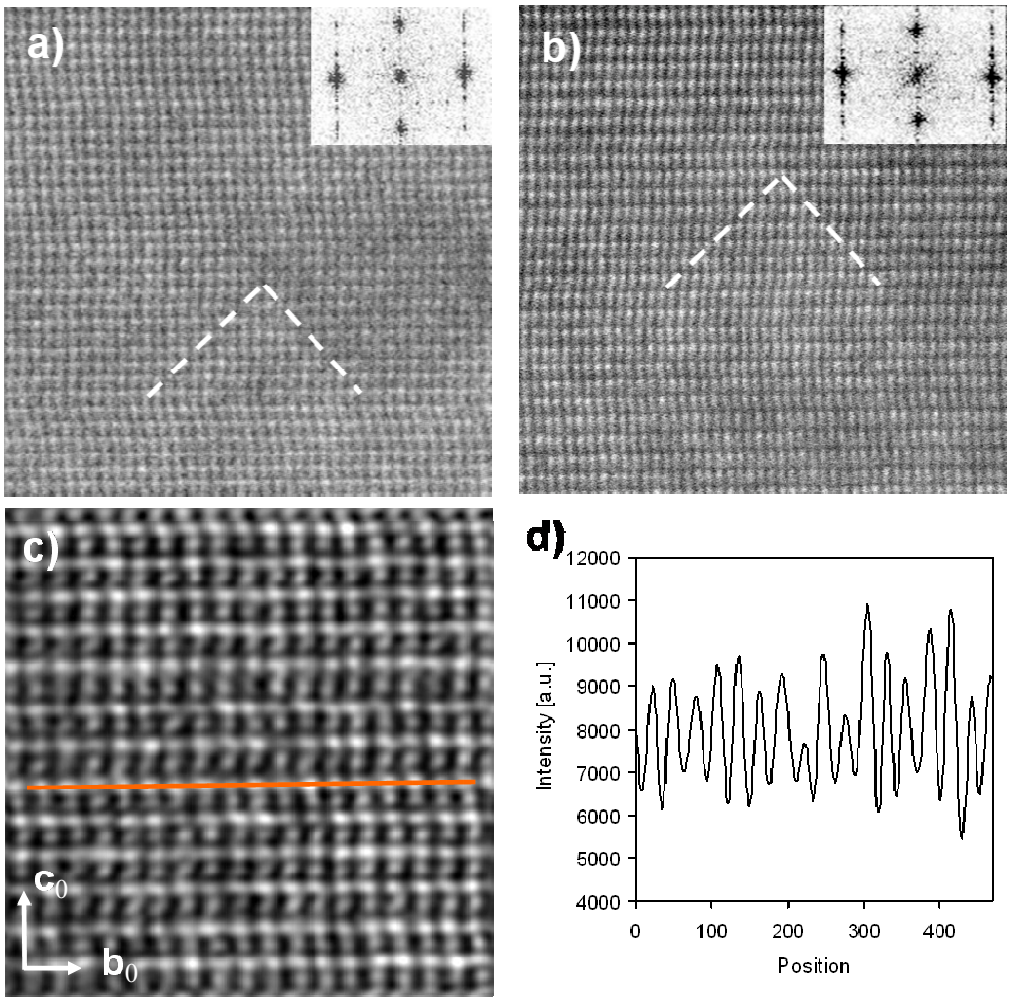

FIG. 3. (Color online) *Z*-contrast STEM images in $Pr_{0.5}Ca_{0.5}MnO_3$ with the $2b_0$ superstructure along the [100] direction acquired at collection angles of (a) 119 mrad and (b) 15.5 mrad. The FFT inset shows a slightly weaker superstructure in (a) compared to (b). A thickness-contrast feature, indicated by the white lines, was used as a marker. (c) *Z*-contrast STEM image of the same area with higher spatial resolution (low-pass filtered) and (d) line profile of a Pr/Ca column taken as indicated by the line in (c).

C. Topology of the $2b_0$ charge-ordered and/or orbital-ordered superstructure

As a starting point for our analysis of the $2b_0$ superstructure, we checked the structural model for the disordered phase. For both selected doping values, the diffraction patterns along the [001], [010], [100], and [110] zone axes can be excellently described by space group *Pbnm* (No. 62), with a refinement for the coordinates obtained by the neutron diffraction study of Jirák *et al.*[9]

For modeling of the underlying lattice distortions that generate the $b_s=2b_0$ superlattice modulation, we checked all possible subgroups of the disordered phase with *Pbnm* symmetry. Only $P2_1nm$ (No. 31), which was used by Daoud-Aladine *et al.* to refine the ordered phase,[20] complies with the general reflection conditions that we determined. In the space group *Pbnm*, the diagonal glide plane *n* [which is defined by the $y=\frac{1}{4}$ plane and the glide vector $(\frac{1}{2}, 0, \frac{1}{2})$] causes the extinction for $h0l$ reflections with $h+l=2n+1$. This diagonal glide plane is inherited by the space group $P2_1nm$. In contrast, the other glide plane *b* in *Pbnm* [defined by the $x=\frac{1}{4}$ plane and the glide vector $(0, \frac{1}{2}, 0)$], which results in the extinction of $0kl$ reflections with $k=2n+1$, is lost in $P2_1mn$. However, this extinction still exists in the ordered phase that is $k/2=2n+1$ in the superlattice whose unit cell doubles along the *b* axis [see Figs. 2(c) and 2(d)]. This implies that the *b* glide plane still remained locally in the $2b_0$ ordered phase, at least along the *b* and *c* directions. In other words, the atoms form pairs in which they have local *b*-glide-plane symmetry. By extending the local *b* glide plane to the *a* direction, for each pair, the following rules are obtained: if the coordinate of the first atom is x, y, z, then the coordinate of the second atom is $-x+1/2$, $y+1/4$, z, accordingly; if the displacement of the first atom is Δ_x, Δ_y, and Δ_z, then that of the second atom is $-\Delta_x$, Δ_y, and Δ_z. We will discuss the consequence of breaking the local *b*-glide-plane symmetry in the *a* direction in Sec. III E. To build the atomic model of the ordered phase, we started from the Wyckoff positions transformed from the disordered phase,[9] then modified the position by introducing a displacement vector Δ_i for each position. The modified Wyckoff position X_i is given by

TABLE I. Wyckoff coordinates A_x, A_y, A_z of the disordered state (space group *Pbnm*) described within the $P2_1nm$ setting for $x=0.50$. A translation of $t=[0,-0.125,0.25]$ allows coincidence with the *Pbnm* setting of Jirak *et al.* (Ref. 9).

	Wyckoff position of disordered state			Displacement of the model of Daoud-Aladine *et al.*[a]			Displacement of our ZP-CO/OO model		
Atom	A_x	A_y	A_z	Δ_x	Δ_y	Δ_z	Δ_x	Δ_y	Δ_z
Pr/Ca	−0.006	0.14	0	−0.0023	0.0031	0	0	0	0
Pr/Ca	0.506	0.39	0	−0.0095	0.0017	0	0	0	0
Pr/Ca	−0.006	0.64	0	−0.0216	−0.0009	0	0	0	0
Pr/Ca	0.506	0.89	0	0.0121	0.0041	0	0	0	0
$O_{I,1}$	0.43	0.1165	0	0.0053	−0.006	0	0.008	−0.005	0
$O_{I,2}$	0.07	0.3665	0	−0.0138	0.0073	0	−0.008	−0.005	0
$O_{I,3}$	0.43	0.6165	0	−0.0196	−0.0031	0	−0.008	0.005	0
$O_{I,4}$	0.07	0.8665	0	0.0043	−0.0006	0	0.008	0.005	0
Mn_I	0.5	0.125	0.75	0	−0.0006	−0.0011	0.015	0	0
Mn_{II}	0	0.375	0.75	−0.0205	−0.0004	−0.0008	−0.015	0	0
$O_{II,1}$	0.217	0.233	0.714	−0.0018	0.0013	0.0118	0.004	0.003	0.003
$O_{II,2}$	0.283	0.483	0.714	−0.0355	−0.0006	0.008	−0.004	0.003	0.003
$O_{II,3}$	0.217	0.733	0.714	−0.004	0.0009	0.0079	0.01	−0.005	−0.005
$O_{II,4}$	0.283	0.983	0.714	0.0174	0.003	0.0109	0.01	−0.005	−0.005

[a]Reference 20.

$$X_i = A_i + \Delta_i,$$

where $A_i=(A_{x,i},A_{y,i},A_{z,i})$ represents the Wyckoff positions of the disordered *Pbnm* phase in the superlattice axes. Apparently, the $P2_1nm$ symmetry collapses into the *Pbnm* symmetry if all $\Delta_i=0$. If Δ_i complies with local *b*-glide-plane symmetry, the new atomic position X_i keeps local *b*-glide-plane symmetry as well. Table I lists the Wyckoff positions A_i for the disordered *Pbnm* phase as refined by Ref. 9 for $x=0.50$, and Δ_i is calculated from the ZP model of Daoud-Aldine *et al.* with the $P2_1nm$ space group.[20] It shows that the atomic displacements in the model of Daoud-Aladine *et al.* do not comply with the local *b*-glide-plane symmetry, and thus, may not obey the reflection condition we observed in the $0kl$ reflections. Dynamic electron-diffraction calculations based on the Bloch-wave theory substantiate this conclusion. Figure 2(g) shows the simulated electron-diffraction pattern based on the model of Daoud-Aladine *et al.* The reflections with $k/2=2n+1$ are visible. The simulated diffraction, instead, is very similar to Fig. 2(e), which contains both [100] and [010] domains.

Before building the superstructure model, it is important to understand how the displacement of atoms affects the basic features of the structure. In particular, it was necessary to determine the static cooperative JT modes that are compatible with the diffraction and EELS results, and thus, determine the electronic structure and physical properties of the materials. For simplicity, we will only discuss the MnO plane that involves the Mn and O_{II} atoms since they have the most influence on the JT distortions. Figures 4(a) and 4(b), respectively, show the three-dimensional (3D) model and the [001] projection of the disordered phase in the superstructure directions. In the $P2_1nm$, there are four symmetric operators [see Figs. 4(a) and 4(b)] that transform one Wyckoff position to four equivalent atoms (we draw these equivalent positions in the same color). As we discussed before, the additional extinction in $0kl$ requires the atoms to form pairs. Although there are totally 12 pairs in the MnO plane, by combining the pairs linked by the $P2_1mn$ symmetry, there are actually only three independent pairs, which are the Mn_I and Mn_{II} pair, $O_{II,1}$ and $O_{II,2}$ pair, and $O_{II,3}$ and $O_{II,4}$ pair, respectively. First, we fixed Mn ($\Delta_{Mn}=0$) and considered the superstructures due to the displacement of the O_{II}. In this case, the angle of Mn_I-$O_{II,1}$-Mn_{II} and that of Mn_{II}-$O_{II,2}$-Mn_{II} are the same, since $O_{II,1}$ and $O_{II,2}$ are coupled by the local *b*-glide-plane symmetry, while the Mn_{II}-$O_{II,3}$-Mn_I angle and the Mn_I-$O_{II,4}$-Mn_I angle also are the same. The Mn_I-$O_{II,1}$-Mn_{II} angle may increase due to the displacement of $O_{II,1}$, e.g., the displacement of $O_{II,1}$ along $+x+y+z$ direction (denoted as +++). The corresponding displacement of $O_{II,2}$ (e.g., −++), defined by local *b*-glide-plane symmetry, then results in the same increase of the Mn_{II}-$O_{II,2}$-Mn_{II} angle. The pair $O_{II,3}$ and $O_{II,4}$ is independent of the first $O_{II,1}$ and $O_{II,2}$ pair. If the second pair is moved in the same way to increase the Mn_{II}-$O_{II,3}$-Mn_I and Mn_I-$O_{II,4}$-Mn_I angles, we basically obtain a global *b* glide plane, and therefore, end up with a structure similar to that of the disordered phase without superlattice reflections and oxygen prepeak oscillations along the *b* direction. Moving $O_{II,3}$ and $O_{II,4}$ in the opposite way (e.g., −−− for $O_{II,3}$, +−− for $O_{II,4}$) decreases the Mn_{II}-$O_{II,3}$-Mn_I and Mn_I-$O_{II,4}$-Mn_I angles. Figure 5(a) depicts the changes of the Mn-O_{II}-Mn bonding angle and the average Mn-O_{II} bonding length with the amplitude of displacement. In contrast, moving O_{II} atoms in the opposite way will decrease the Mn_I-$O_{II,1}$-Mn_{II} and Mn_{II}-$O_{II,2}$-Mn_{II} angles,

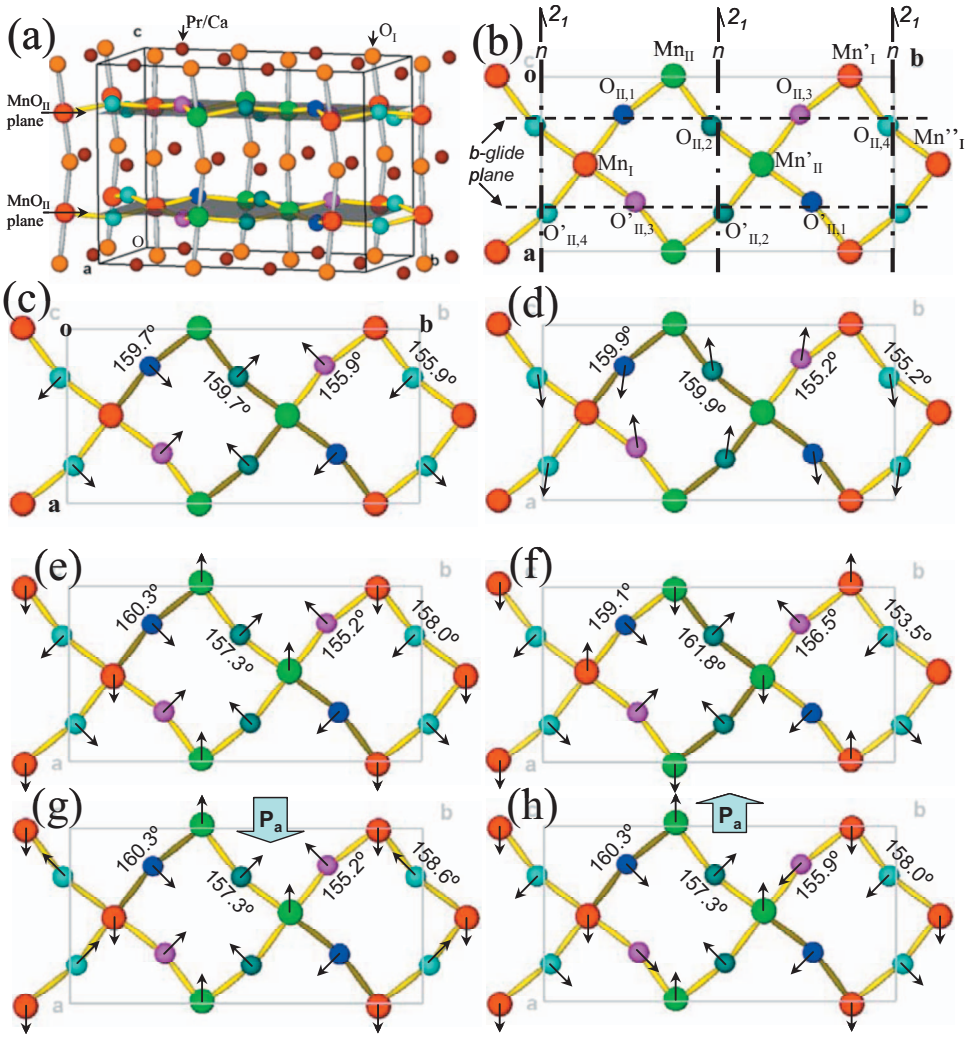

FIG. 4. (Color) (a) A 3D view and (b) the [001] projection of the disordered phase. (c)–(h) The [001] projections of the ordered phases. For simplicity, the Pr/Ca and O_I atoms are not included. (c) CO and/or OO trimer state ($\Delta_{Mn}=0$, $\Delta_{OII}=0.0025$). (d) CO and/or OO trimer state with different displacement amplitudes along the *a*, *b*, and *c* directions. (e) CO and/or OO Zener polaron state ($\Delta_{Mn}=0.015$, $\Delta_{OII}=0.0025$). (f) CO and/or OO dimer-chain state ($\Delta_{Mn}=-0.015$, $\Delta_{OII}=0.0025$). (g) Same as (e) but with a reverse displacement of the $O_{II,4}$ along the *a* direction ($\Delta^x_{OII,3}=\Delta^x_{OII,4}=-0.0025$), resulting in a net electric polarization along the *a* direction. (h) Same as (e) but with a reverse displacement of the $O_{II,3}$ along the *a* direction ($\Delta^x_{OII,3}=\Delta^x_{OII,4}=0.0025$), resulting in a net electric polarization along the $-a$ direction. The black arrows represent the in-plane displacement.

while increasing the angles of Mn_{II}-$O_{II,3}$-Mn_I and Mn_I-$O_{II,4}$-Mn_I. This leads us to get the same structure but moving the unit cell by $\frac{1}{2}$ b_s. In conclusion, without moving Mn, after moving O_{II} by a certain amount, the Mn-O_{II}-Mn bonds split into two Mn-O-Mn-O-Mn trimers as shown in Fig. 4(c). One (Mn_I-$O_{II,1}$-Mn_{II}-$O_{II,2}$-$Mn_{II'}$) has large bonding angle and slightly short bonding length that cause strong ferromagnetic (FM) coupling of the Mn atoms; the other ($Mn_{II'}$-$O_{II,3}$-$Mn_{I'}$-$O_{II,4}$-$Mn_{I''}$), with a small bonding angle and slightly large bonding length, suppresses FM exchange. The trimer formation is related to the differentiation of the bonding lengths, and thus, leads to orbital ordering. Judging by the bond-valence sum and the dependence of the e_g bandwidth on the Mn-O-Mn bonding angle, we conclude that the valence disproportionation between Mn_I and Mn_{II} is much less than 1*e*; however, the e_g electrons preferentially occupy a chainlike pattern formed by the trimer arrangement. Consequently, we refer this state as a CO and/or OO trimer, with a bond-centered type of CO. To some extent, these trimer chains could behave as a one-dimensional metal.

This general qualitative picture, where we used the same amplitude Δ_i along the *x*, *y*, and *z* directions, does not change much if the amplitudes along *x*, *y*, and *z* are different. For example, the $O_{II,1}$ may move along +−−, and the amplitude along *x* is significantly larger than those along the *y* and *z* directions; this also increases Mn-$O_{II,1}$-Mn angle. By applying local *b*-glide-plane symmetry, the Mn-$O_{II,2}$-Mn angle increases as well, while those of Mn-$O_{II,3}$-Mn and Mn-$O_{II,4}$-Mn decrease. So the CO and/or OO trimer is preserved. In addition to the described rotational JT modes, the local *b* glide plane allows for an approximation of the out-of-phase stretching-type modes of the in-plane O_{II} [see Fig. 4(d), where Δ_{OII} are +−−, −−−, −++, and +++]. Again, a $2b_0$ superlattice can be produced only if the global *b*-glide-plane symmetry is broken, i.e., the *b* glide plane between pairs 1 and 2, and 3 and 4 is broken, and the resulting qualitative structure shows orbital ordering with a very small trimer-type variation of the Mn-O-Mn bonding angles and negligible CO (this is true for both the site and bond-centered types of CO).

Now let us examine the effect of moving Mn atoms. For the dynamic JT distortion, the Mn displacements are thought to be present in A_g-type rotational modes.[43] We started from the CO and/or OO trimer state with the O_{II} displacement being 0.0025 (hereafter, the displacement is described using a fraction of the unit-cell length, where $a=0.5395$ nm, $b=1.0622$ nm, and $c=0.7612$ nm) and only moved the Mn along the *a* direction (because our STEM observations did not reveal displacements along the *b* and *c* directions). Since

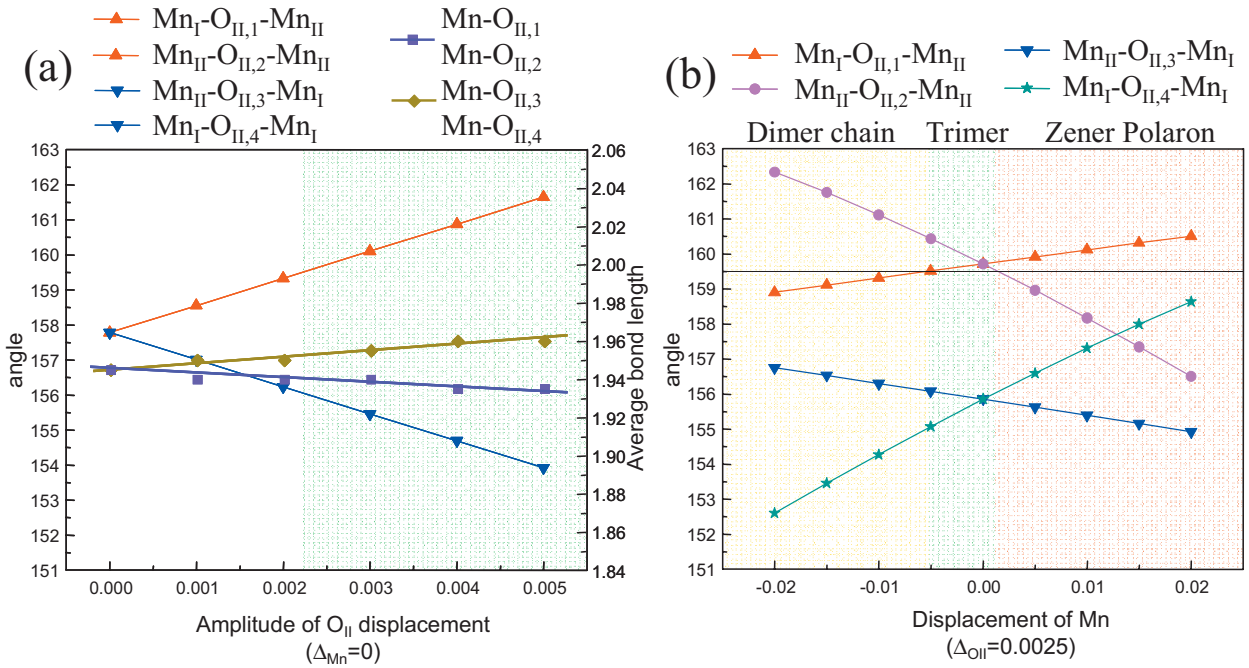

FIG. 5. (Color) (a) Changes of Mn−O$_{II}$−Mn bonding angles and Mn−O$_{II}$ bonding length against the displacement of O$_{II}$ with Δ_{Mn}=0. The moving directions are +++, −++, −−− and +−− for O$_{II,1}$, O$_{II,2}$, O$_{II,3}$, and O$_{II,4}$, respectively. For convenience, we use the same amplitude for all O$_{II}$. (b) Profiles of Mn−O$_{II}$−Mn bonding angles vs displacement of Mn with Δ_{OII}=0.0025. The ordered phase can be divided into three categories based on the displacement of Mn. The green shaded area is considered as a CO and/or OO trimer, the pink as a CO and/or OO Zener polaron, and the yellow as the CO and/or OO dimer chain, respectively. A 159.5° critical angle was used to distinguish the states.

Mn$_I$ and Mn$_{II}$ are paired, moving Mn$_I$ along the $+x$ direction also results in Mn$_{II}$ moving along $-x$, thus increasing the Mn$_I$-O$_{II,1}$-Mn$_{II}$ and Mn$_I$-O$_{II,4}$-Mn$_I$ bonding angles, while decreasing the Mn$_{II}$-O$_{II,2}$-Mn$_{II}$ and Mn$_{II}$-O$_{II,3}$-Mn$_I$ angles, as shown in Fig. 5(b). Supposing that 159.5° is the critical angle for Mn-O$_{II}$-Mn bonding that changes the bonding state,[31] then in the pink shaded area where the displacement of Mn is more than 0.001, the Mn$_I$-O$_{II,1}$-Mn$_{II}$ bonding angle and Mn-O$_{II,1}$ bonding length become significantly larger than the others, similar to the model proposed by Daoud-Aladine *et al.*. We refer this as the CO and/or OO ZP state, as shown in Fig. 4(e). Moving Mn in the opposite way de-

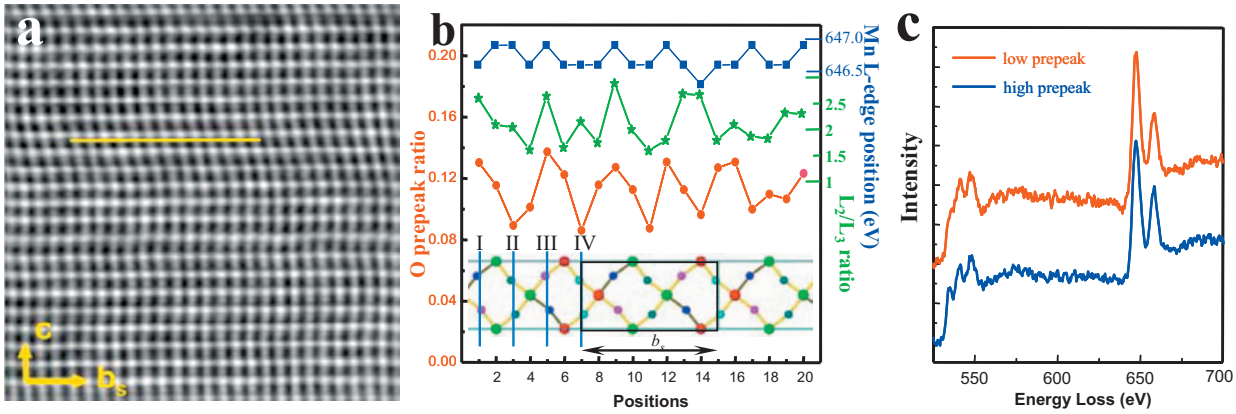

FIG. 6. (Color) (a) Low-pass filtered *Z*-contrast STEM image of $Pr_{0.5}Ca_{0.5}MnO_3$ along the [100] direction, showing a $2b_0$ ordered area confirmed by HRTEM and SAED. (b) Results of 20 EELS scans taken equidistantly along the line indicated in (a) with eight acquired spectra per b_s lattice parameter, showing Mn *L*-edge onset position, $L_{2,3}$ ratio, and O-prepeak ratio. The MnO$_{II}$ plane with Zener polaron state is shown at the bottom, where I–IV indicate individual atomic columns for different O$_{II}$ sites with incident electrons passing from top to the bottom in this plane. While the variation of the Mn *L*-edge position is within the measurement error, there is a significant variation in the relative O$_{II}$ prepeak, revealing the presence of nonequivalent O$_{II}$ positions with a twofold modulation in the b_s supercell. The spatial variation of the L_2/L_3 ratio shows the same periodicity and is correlated to the prepeak oscillation. The EELS spectra for positions larger than 15 are distorted by noise due to the increase of contamination of the probed area while acquiring of the spectra. (c) Two typical spectra of the line scan, with a high and a low O prepeak, respectively.

creases the Mn_I-$O_{II,1}$-Mn_{II} and Mn_I-$O_{II,4}$-Mn_I bonding angles, while increasing the Mn_{II}-$O_{II,2}$-Mn_{II} and Mn_{II}-$O_{II,3}$-Mn_I bonding angles. In the yellow shaded area where the displacement of Mn is less than −0.005, the Mn_{II}-$O_{II,2}$-Mn_{II} bonding angle becomes significantly larger than the others. The Mn-$O_{II,2}$-Mn-$O_{II,2}$-Mn forms a dimer chain along the a direction, as shown in Fig. 4(f). Again, these chains represent the preferential bonds for the distribution of the e_g electrons, and we refer to them as the CO and/or OO dimer chain with bond-centered type of CO.

From the above discussion, it is clear that the displacement of Mn plays a key role in determining the feature of the $2b_0$ superstructure. In the green shaded area in Fig. 5(b) where the displacement of Mn is small, the ordered phase has a CO and/or OO trimer state. In the pink shaded area, the ordered phase has a CO and/or OO Zener polaron state, while in the yellow shaded area, it has a CO and/or OO dimer-chain state.

D. Electron energy-loss spectroscopy

The electronic structure and environment at the O_{II} and Mn sites along the b axis (see Fig. 4) are different for trimer and dimer chains and Zener polaron states, and therefore, may be distinguished by a series of atomic-column-resolved EELS spectra shown in Fig. 6. The physical principle behind EELS relates the interaction of fast electrons with the sample to cause either collective excitations of electrons in the conduction bands (plasmons) or discrete transitions between atomic energy levels.[40] In this study, we focus on the latter class, using oxygen K edge and Mn L edge core-loss spectra, which were acquired with a convergence angle of 11 mrad and a collection angle of 28 mrad. The spectra shown here are background subtracted, but not deconvoluted with the zero-loss peak. A series of 20 spectra was acquired at different positions along the b_s axis, such that eight spectra at distances of 1.3 Å were recorded within a period of the superlattice b_s. The electron beam was lying in the MnO_{II} plane [see Fig. 4(a)] and parallel to the [100] axis, therefore probing atomic columns along the crystallographic a axis. Using HRTEM, SAED, and MAADF imaging, a particular area was selected for the STEM and EELS experiments, where it was confirmed that it has a large domain with the $b_s=2b_0$ superstructure.

Figure 6(c) shows two typical spectra in the energy range between 525 and 700 eV, with the O K edge located at 532 eV, and the onset of the manganese $L_{2,3}$ edges at 640 eV, respectively. The O K edge contains three characteristic peaks, the prepeak at 532 eV and then the two main peaks at 540 and 547 eV, while the Mn L edge consists of the L_3 and L_2 edges at 647 and 657 eV, respectively. Comparing the EELS spectra of the line scan along the b_s direction, we found strong periodic oscillations of the oxygen prepeak intensity with a periodicity of half the b_s-axis supercell [Fig. 6(b)]. On the other hand, the L_3-edge onset appears unchanged along the entire line scan, within the measurement error (all the spectra were aligned with respect to the O K-edge onset at 532 eV). Interestingly, there is an oscillation of the L_3,L_2 intensity ratio that, to some degree, correlates with variations in the oxygen prepeak intensity. (The EELS spectra at positions above 15 become noisier due to the increasing carbon contamination of the sample while acquiring the spectra.) We have repeated the EELS experiments in several different areas, and obtained reproducible results. We note that the oscillations were often more periodic during the first dozens of second acquisition, largely due to the clean surface and negligible sample drift.

The above results can be best understood by considering the different kinds of information revealed from the O K edge and Mn L edges. The O K edge probes transitions from the O $1s$ states into the unoccupied $2p$ states, which are hybridized with the Mn $3d$ and $4sp$ states.[45] Although these transitions involve oxygen orbitals, the O K-edge fine structure, in particular, its prepeak intensity, is mainly determined by the electronic structure of the $3d$ transition-metal ions. This is due to the fact that the valence of the transition-metal ion, or correlation effects in the transfer of electrons to the cation, changes the degree of hole doping on the oxygen p states, resulting in a relative change in the O prepeak intensity.[46] Our preliminary density functional theory calculations show that the intensity of the O prepeak increases with the increase of the Mn-O-Mn bonding angle.

The Mn L_3 and L_2 peaks (located at 647 and 658 eV) are the result of transitions from the $2p^{1/2}$ and $2p^{3/2}$ Mn core-level states to the unoccupied d-like states, modified by crystal-field and electron-spin interactions. Changes in both the Mn L-edge positions as well as in the L_2/L_3 intensity ratio have been correlated with the formal Mn valence in various MnO_x compounds,[45,47] and also have been frequently utilized to obtain information about the valence state and p-d hybridization of MnO_6 octahedra in manganites.[48] By comparing several different MnO_x compounds, it was previously shown that the Mn L_3-edge position shifts by 2.5 eV from a formal Mn^{3+} to Mn^{4+} valence state.[47,49] Similarly, a change in the L_3/L_2 ratio from 2.7 to 2.0 for Mn^{3+} and Mn^{4+} has been previously reported.[47]

The three different configurations of the $2b_0$ superstructure we discussed in Sec. III C can now be examined by the variation of the oxygen K-edge prepeak intensity along the b direction. For a trimer state [Fig. 4(c)], column II [see Fig. 6(b)] involves two Mn-$O_{II,2}$-Mn dimers that have large bonding angles, and therefore should have the highest O prepeak, while column IV goes through two Mn-$O_{II,4}$-Mn dimers with small bonding angles, and should have the lowest O prepeak. For columns I and III, the mixed Mn-$O_{II,1}$-Mn and Mn-$O_{II,3}$-Mn dimers with large and small bonding angles, respectively, results in an intermediate O-prepeak intensity. Thus, the periodicity of the O prepeak for a trimer state is b_s. Similarly, the periodicity of the O prepeak for a dimer chain model [Fig. 4(f)] is b_s. These configurations do not agree with the observation of $\frac{1}{2}$ b_s periodicity of the O prepeak shown in Fig. 6(b). In contrast, for the Zener polaron model [Fig. 4(e)], the bonding angle of the Mn-$O_{II,1}$-Mn dimer is significantly larger than the others, therefore columns I and III exhibit a high intensity of O prepeak, while columns II and IV that only involve dimers with small bonding angles exhibit a low O prepeak. Thus, the periodicity of the O prepeak is $\frac{1}{2}$ b_s, which is in agreement with the experiment.

Thus, from the column-by-column EELS data in Fig. 6(b), the following conclusion can be reached: The variation

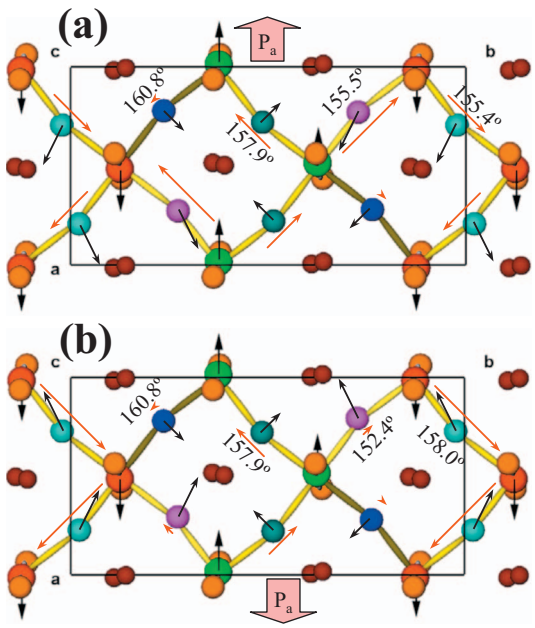

FIG. 7. (Color) (a) Refined ZP-CO/OO model with net electric polarization P_a=−44 mC/m^2 (coordinators from Table I). (b) ZP-CO/OO model obtained by reversing $\Delta^x_{\mathrm{OII,3}}$ and $\Delta^x_{\mathrm{OII,4}}$ that, in turn, reverses the net electric polarization P_a. The black arrows represent the in-plane displacement. The in-plane electric dipole moments **P** of the Mn-O-Mn dimers determined from the noncentrosymmetric atomic displacements are indicated by red arrows. The length of the arrows corresponds to the magnitude of the displacement or the polarization. The color index from yellow to cyan for the orbitals reflects the increasing bond angle of the Mn-O-Mn dimer, which results in an enhancement of the ferromagnetic double exchange and increases orbital occupation by the e_g electrons.

of the oxygen *K*-edge prepeak ratio clearly proves that nonequivalent oxygen sites with different hole-doping levels are present along the crystallographic *b* axis in the ordered state. The observed periodicity of b_0 (instead of $2b_0$) directly confirms the ZP-type structure and rules out the trimer type of CO and/or OO stripes and the dimer-chain state. Moreover, the absence of any shift L_3-edge onset is consistent with the absence of strong charge disproportionation. This supports the configuration of the ZP-CO/OO. On the other hand, the origin of the observed strong oscillation in the manganese L_3/L_2 intensity ratio is more complex since the intensity of white lines (L_3 and L_2 edges) of a 3*d* transition element depends not only on its electronic environment, but also strongly on its spin orbital and configuration, which are the foundation for x-ray magnetic circular dichroism experiments. Although the changes in the L_3/L_2 ratio are used to interpret the valence on Mn (Mn^{3+} and Mn^{4+}) in pure manganese oxides, we proposed that the changes we observed here are mainly due to the difference in spin configuration and interactions of the nonequivalent Mn_I and Mn_{II} sites as well as the difference in the orbital configurations and population, rather than to a change in the Mn valence or an effect of charge transfer. This interpretation is consistent with the measured modulation of the O *K*-edge prepeak, our diffraction data, and the asymmetric electronic configuration of the ZP Mn-O-Mn dimer.

E. Electric polarization

The observation of ferroelectric domains and the decrease of the low-frequency part of the dielectric permittivity in an electrically induced ZP disorder transition require that the net electric polarization **P** be reversible.[50] Based on the noncentrosymmetric distortions of the oxygen anions, the electric polarization **P** introduced by the noncentrosymmetric Mn-O-Mn dimer can be calculated by $\mathbf{P}=(q_{\mathrm{Mn}}-q_{\mathrm{O}})(b_2-b_1)$, where b_i are the bond lengths and q_i are the ionic charges of the O and Mn ions. Because the valence difference among Mn atoms is very small, the first term is almost constant for all Mn-O-Mn dimers, and therefore, **P** basically depends on the noncentrosymmetric displacement of atoms. Due to the 2_1 screw axis of the $P2_1nm$ space group, the *b* and *c* components of **P** cancel each other out, i.e., are zero. For example, if one atom (say, atom 1) has a displacement of Δ_x, Δ_y, and Δ_z, then the other atom (atom 2) related by the 2_1 screw axis would have the displacement of Δ_x, $-\Delta_y$, and $-\Delta_z$. The components *b* and *c* of the polarization caused by the displacement of atom 1 will therefore be cancelled by that of atom 2. The $P2_1nm$ space group does allow the *a* component of electric polarization, P_a. However, if all three pairs (Mn_I and Mn_{II}, $O_{II,1}$ and $O_{II,2}$, and $O_{II,3}$ and $O_{II,4}$) have local *b*-glide-plane symmetry, the total P_a over the supercell also would be zero since the P_a caused by the first atom in the pair will be cancelled by the second atom in the same pair because their displacement along the *a* direction is reversed. It is, therefore, necessary to break the local *b*-glide-plane symmetry in the *a* direction to obtain net P_a. Breaking the local *b*-glide-plane symmetry of either the Mn_I and Mn_{II} pair, or the $O_{II,1}$ and $O_{II,2}$ pair in the ZP CO/OO supercell [Fig. 4(e)] can yield net P_a along the $-a$ direction. This can be done by either only moving Mn_{II} to $-x$, or moving both $O_{II,1}$ and $O_{II,2}$ to $+x$. However, we cannot yield P_a along $+a$ direction while keeping the ZP feature since it would give rise to a trimer chain. This is unlikely, and also inconsistent with our dielectric experiments[50] using electron holography, and would lead to a behavior where a sign reversal of an applied electric field could switch between an insulating ZP-CO/OO state and a one-dimensional metal (trimer) just by reversing P_a. To obtain a reversible P_a while keeping the ZP feature, it is necessary, however, to break the local *b*-glide-plane symmetry of the third pair ($O_{II,3}$ and $O_{II,4}$ pair) in the *a* direction. Figure 4(g) shows the example with P_a along the $+a$ direction. The difference between Figs. 4(g) and 4(e) is that $O_{II,3}$ and $O_{II,4}$ in the third pair both move to $-x$ in the *a* direction in Fig. 4(g). It is the breaking of local *b*-glide-plane symmetry in the *a* direction of the third pair yields the net P_a. By reversing the displacement of the third pair to $+x$, we get $-P_a$ while still keeping the ZP feature [Fig. 4(h)]. Consequently, this model is consistent with a ZP-CO/OO state that exhibits a true ferroelectric behavior. We note that breaking the local *b*-glide-plane symmetry along the *a* direction is still compatible with the extinction rule observed in the [100] zone axis.

IV. DISCUSSION

Based on our electron diffraction, *Z*-contrast imaging, and atomic resolution EELS analysis and the observation of

ferroelectric polarization,[50] we find that only one configuration, the CO and/or OO Zener polaron structure with reversible net electric polarization, is consistent with all experimental observations. By refining electron diffraction, we obtained our Zener polaron model [Fig. 7(a)]. Table I lists the displacement of atoms. It represents a bond-centered type of charge ordering, where the e_g electrons are localized in preferential Mn-O-Mn bonds and the bonding angle of which is increased from 157.8° to 160.8° (for $x=0.50$). This model can nicely explain the colossal electroresistance effect as an order-disorder transition of statically ordered ZP to dynamic JT polarons by an applied electric field and current.[50] Furthermore, the observation of a local b-glide-plane symmetry by the presence of an additional extinction rule for the $0kl$ reflections, with $k/2=2n+1$, gives us much insight into the involved A_g JT modes. By keeping local b-glide-plane symmetry and reversing some of the displacement amplitudes, a CO and/or OO state can be easily transformed into a trimer-chain structure. This structure could be significant for the understanding of the magnetic-field-induced transition to a ferromagnetic metallic state and the related dominance of e_g-band conduction.

The $P2_1nm$ space group does not allow a pure Mn-site-centered CO state, based on structural arguments: Such a state would require a static centrosymmetric breathing-type modulation of the MnO_6 octahedra, with periodic variations of the average O_{II}-Mn bond lengths for the Mn_I and Mn_{II} sites, in contrast to the glide planes of this space group. The symmetry of this space group unavoidably introduces noncentrosymmetric distortions into the MnO_6 octahedra that tend to create dimer chains of manganese and oxygen. By comparing the superstructure model with the *Pbnm* structure of the C and/or O disordered state, it seems to be possible that a strong octahedral tilting facilitates the formation of this type of CO and/or OO state. Furthermore, the ZP-CO/OO model with dominant bond-centered CO in the Mn-O-Mn dimers is consistent with a small charge disproportionation $\delta \ll 1e$ revealed by RXD[20] and XANES.[22]

A major consequence of the existence of the ZP-CO/OO state that we have determined is the encompassed noncentrosymmetric distortions of the MnO_6 octahedra as well as the Mn-O-Mn dimers. Although, according to the so-called d^0 rule,[51] the filled d-p orbitals of the MnO_6 bonds tend to oppose the formation of noncentrosymmetric distortions by the first-order JT effect; the presence of second-order JT distortions may induce the loss of the centrosymmetry.[8] The associated displacement of the bound positive charges at the Mn cations with respect to the bound electrons of the oxygen anions represents static electric dipoles,[28] which, in turn, form a zigzag long-range-ordered, canted antiferroelectric state. It causes a dipolar electric net moment, P_a, pointing along the crystallographic a axis, whereas P_b sums up to zero, as expected. An estimate of the resulting net polarization depends on the noncentrosymmetric displacements involved and the valence of the ions. Based on the displacements of our ZP-CO/OO model and the assumed valences of the O and Mn atoms of 2− and 3.5+, respectively, we obtain a net-polarization component per unit cell of $P_a \approx 44\ \mathrm{mC/m^2}$. Qualitatively, the presence of polar displacements is determined by the space group; however, the exact quantitative value of the polarization depends on the distortion amplitudes Δ_i. Such a ferroelectric state which becomes multiferroic below T_N is in full agreement with the noncentrosymmetric space group $P2_1nm$. Simply reversing the displacement of $O_{II,3}$ and $O_{II,4}$ along the a direction flips the net polarization along the a direction by 180° and, therefore, gives rise to antiferroelectric domains [Fig. 7(b)]. On macroscopic scales, the net dipolar electric moment is strongly reduced due to strong twinning, antiphase domains in the superstructure, and electronic-phase separation; however, the observed anomalies in the dielectric constant at the CO temperature were recently discussed in terms of the ordering of static moments.[52] The measurement of the net polarization is additionally complicated by the colossal electroresistance in PCMO, wherein the ZP-CO/OO state becomes disordered by the application of electric currents and the related onset of polaron motion. This is probably the main reason that the ferroelectric or canted antiferroelectric behavior is strongly hidden in that material.

We now comment on the relation of our work to other results on CO and/or OO superstructures. Neutron diffraction[53] and TEM[54] studies suggest that the CO transition at half doping is related to the formation of an intermediate state, where the ordering transition to a commensurate low-temperature state occurs via incommensurate modulations for $T_{co} < T < T_N$,[54] however, such observations are not seen in x-ray diffraction studies.[21,55] Within the framework of the conventional CB type of CO and/or OO, the incommensurableness was believed to be formed by π-phase slips of the modulation of the Mn^{3+}/Mn^{4+} sites, the so-called discommensurations.[54] It was considered as stacking faults in the charge crystal that compensate for the charge at other doping ranges, and thereby stabilize a CB-like ordered structure in a wider doping region around $x=0.50$. Our studies show the simultaneous presence of $b_s=2b_0$ and $b_s=3b_0$ at nanometer length scales (see Fig. 1); however, we cannot rule out the presence of incommensurate structures. The observation of the ZP-type CO and/or OO state with a modulation $b_s=2b_0$ in a large doping range of $0.3 \leqslant x \leqslant 0.5$ indicates that there is a very weak link between the hole-doping level and the period of the superstructure modulation. For the ZP-CO/OO state, the real space ordering of e_g electrons is, to a large extent, independent of the average Mn valence state and, thus, of the doping level. In contrast to our observations in PCMO, for $La_{0.48}Ca_{0.52}MnO_3$, the presence of a superlattice with a uniform incommensurate periodicity on the length scale of several nanometers was reported recently by convergent beam electron diffraction.[56]

V. SUMMARY

By careful experiments of electron diffraction from the individual twin domains, combined with atomic-column-resolved EELS, we confirmed the presence of Zener-polaron-type ordering for $Pr_{1-x}Ca_xMnO_3$ in the doping range of $0.3 \leqslant x \leqslant 0.5$ and the temperature window of $300\ \mathrm{K} \geqslant T \geqslant 80\ \mathrm{K}$ both for bulk polycrystalline material and epitaxial thin films. At room temperature, ordered domains with diameters between 10 and 100 nm coexist with disordered areas in a

chemically homogeneous material. Based on the noncentrosymmetric distortions involved in the transition between the *Pbnm* and the $P2_1nm$ space groups for the disordered and ordered states, respectively, we give strong structural evidence for the presence and ordering of static electric dipoles in the ZP-ordered structure. Below T_N, this material, therefore, should exhibit multiferroic ordering. Notably, in addition to the ZP-type CO and/or OO domains with a superlattice period of $b_s=2b_0$ as the dominant ordered area, there are other ordered phases with superlattice modulations of $b_s=3b_0$ and $b_s=5b_0$, on which we will give our comment in an upcoming paper. From a detailed analysis of the electron diffraction patterns from individual and overlapping twins, i.e., using microscopy measurements, we shed light on the possible origins of controversial structure refinements based on volume-averaged macroscopic diffraction measurements. The confirmation of the ZP-CO/OO state strongly impacts our understanding of the interplay of different microscopic interactions for the formation of the insulating ground state, and of its interactions with applied external magnetic and electric fields and the resulting colossal resistance effects.

ACKNOWLEDGMENTS

We thank J. C. Zheng for his stimulating discussions on this project. Funding of the Deutsche Forschungsgemeinschaft (DFG) and SFB 602 is acknowledged by one of the authors (C.J.). Work at Brookhaven National Laboratory was supported by the U.S. Department of Energy, Office of Basic Energy Science, under Contract No. DE-AC02-98CH10886.

*Corresponding author. zhu@bnl.gov
†Corresponding author. jooss@ump.gwdg.de

[1] M. Imada, A. Fujimori, and Y. Tokura, Rev. Mod. Phys. **70**, 1039 (1998).
[2] Y. Tokura, *Colossal Magnetoresistive Oxides* (Gordon and Breach Science, Amsterdam, 2000).
[3] T. A. Kaplan and S. D. Mahanti, *Physics of Manganites* (Kluwer Academic, Dordrecht/Plenum, New York, 1999).
[4] E. Dagotto, *Nanoscale Phase Separation and Colossal Magnetoresistance*, Springer Series in Solid-State Sciences (Springer, New York, 2003).
[5] F. Rivadulla, E. Winkler, J.-S. Zhou, and J. B. Goodenough, Phys. Rev. B **66**, 174432 (2002).
[6] M. W. Lufaso and P. M. Woodward, Acta Crystallogr., Sect. B: Struct. Sci. **B60**, 10 (2004).
[7] E. Dagotto, T. Hotta, and A. Moreo, Phys. Rep. **344**, 1 (2001).
[8] K. M. Ok, N. S. P. Bhuvanesh, and P. S. Halasyamani, Inorg. Chem. **40**, 1978 (2001).
[9] Z. Jirák, S. Krupička, Z. Šimša, M. Dlouhá, and S. Vratislav, J. Magn. Magn. Mater. **53**, 153 (1985).
[10] T. Tonogai, T. Satoh, K. Miyano, Y. Tomioka, and Y. Tokura, Phys. Rev. B **62**, 13903 (2000).
[11] J. P. Hill, C. S. Nelson, M. v. Zimmermann, Y.-J. Kim, D. Gibbs, D. Casa, B. Keimer, Y. Murakami, C. Venkataraman, T. Gog, Y. Tomioka, Y. Tokura, V. Kiryukhin, T. Y. Koo, and S.-W. Cheong, Appl. Phys. A: Mater. Sci. Process. **73**, 723 (2001).
[12] Y. Tomioka, A. Asamitsu, H. Kuwahara, Y. Moritomo, and Y. Tokura, Phys. Rev. B **53**, R1689 (1996).
[13] A. Anane, J.-P. Renard, L. Reversat, C. Dupas, P. Veillet, M. Viret, L. Pinsard, and A. Revcolevschi, Phys. Rev. B **59**, 77 (1999).
[14] W. Westhäuser, S. Schramm, J. Hoffmann, and C. Jooss, Eur. Phys. J. B **53**, 323 (2006).
[15] A. Asamitsu, Y. Tomioka, H. Kuwahara, and Y. Tokura, Nature (London) **388**, 50 (1997).
[16] M. Fiebig, K. Miyano, Y. Tomioka, and Y. Tokura, Science **280**, 1925 (1998).
[17] Y. Moritomo, H. Kuwahara, Y. Tomioka, and Y. Tokura, Phys. Rev. B **55**, 7549 (1997).
[18] V. G. Prokhorov, G. G. Kaminsky, and V. S. Flis, Low Temp. Phys. **25**, 792 (1999).
[19] J. B. Goodenough, Phys. Rev. **100**, 564 (1955).
[20] A. Daoud-Aladine, J. Rodríguez-Carvajal, L. Pinsard-Gaudart, M. T. Fernández-Díaz, and A. Revcolevschi, Phys. Rev. Lett. **89**, 097205 (2002).
[21] S. Grenier, J. P. Hill, D. Gibbs, K. J. Thomas, M. v. Zimmermann, C. S. Nelson, V. Kiryukhin, Y. Tokura, Y. Tomioka, D. Casa, T. Gog, and C. Venkataraman, Phys. Rev. B **69**, 134419 (2004).
[22] J. García, M. C. Sánchez, G. Subías, and Javier Blasco, J. Phys.: Condens. Matter **13**, 3229 (2001).
[23] R. J. Goff and J. P. Attfield, Phys. Rev. B **70**, 140404(R) (2004).
[24] V. I. Anisimov, I. S. Elfimov, M. A. Korotin, and K. Terakura, Phys. Rev. B **55**, 15494 (1997).
[25] C. de Graaf, C. Sousa, and R. Broer, Phys. Rev. B **70**, 235104 (2004).
[26] G. Zheng and C. H. Patterson, Phys. Rev. B **67**, 220404(R) (2003).
[27] C. H. Patterson, Phys. Rev. B **72**, 085125 (2005).
[28] D. V. Efremov, J. van den Brink, and D. I. Khomskii, Nat. Mater. **3**, 853 (2004).
[29] J. C. H. Spence and J. M. Zuo, *Electron Microdiffraction* (Plenum, New York, 1992).
[30] I. D. Brown and D. Altermatt, Acta Crystallogr., Sect. B: Struct. Sci. **B41**, 244 (1985).
[31] J. B. Goodenough and J.-S. Zhou, J. Supercond. **13**, 989 (2000).
[32] J. L. Garcıa-Munoz, J. Fontcuberta, M. Suaaidi, and X. Obradors, J. Phys.: Condens. Matter **8**, L787 (1996).
[33] S. J. Pennycook and L. A. Boatner, Nature (London) **336**, 565 (1988).
[34] R. F. Loane, P. Xu, and J. Silcox, Ultramicroscopy **40**, 121 (1992).
[35] S. Hillyard, R. F. Loane, and J. Silcox, Ultramicroscopy **49**, 14 (1993).
[36] A. Amali and P. Rez, Microsc. Microanal. **3**, 28 (1997).
[37] E. M. James and N. D. Browning, Ultramicroscopy **78**, 125 (1999).
[38] P. D. Nellist and S. J. Pennycook, Proceedings of Microscopy and Microanalysis **5**, 315 (1999).
[39] R. F. Klie and Y. Zhu, Micron **36**, 219 (2005).
[40] R. F. Egerton, *Electron Energy Loss Spectroscopy in the Electron*

Microscope (Plenum, New York, 1986).
[41] J. Fertig and H. Rose, Optik (Jena) **59**, 407 (1981).
[42] N. D. Browning, M. F. Chisholm, and S. J. Pennycook, Nature (London) **366**, 143 (1993).
[43] M. V. Abrashev, J. Backstrom, L. Borjesson, M. Pissas, N. Kolev, and M. N. Iliev, Phys. Rev. B **64**, 144429 (2001).
[44] V. Moshnyaga, L. Sudheendra, O. I. Lebedev, S. A. Köster, K. Gehrke, O. Shapoval, A. Belenchuk, B. Damaschke, G. van Tendeloo, and K. Samwer, Phys. Rev. Lett. **97**, 107205 (2006).
[45] H. Kurata and C. Colliex, Phys. Rev. B **48**, 2102 (1993).
[46] J. van Elp and A. Tanaka, Phys. Rev. B **60**, 5331 (1999).
[47] J. H. Paterson and O. L. Krivanek, Ultramicroscopy **32**, 319 (1990).
[48] M. Varela, T. J. Pennycook, W. Tian, D. Mandrus, S. J. Pennycook, V. Pena, Z. Sefrioui, and J. Santamaria, J. Mater. Sci. **41**, 4389 (2006).
[49] J. H. Rask, B. Miner, and P. R. Buseck, Ultramicroscopy **21**, 321 (1987).
[50] Ch. Jooss, L. Wu, T. Beetz, R. Klie, M. Beleggia, M. Schofield, S. Schramm, J. Hoffmann, and Y. Zhu, Proc. Natl. Acad. Sci. U.S.A. **104**, 13597 (2007).
[51] N. A. Hill, J. Phys. Chem. B **104**, 6694 (2000).
[52] S. Mercone, A. Wahl, A. Pautrat, M. Pollet, and C. Simon, Phys. Rev. B **69**, 174433 (2004).
[53] R. Kajimoto, H. Yoshizawa, Y. Tomioka, and Y. Tokura, Phys. Rev. B **63**, 212407 (2001).
[54] S. Mori, T. Karsufuji, N. Yamamoto, C. H. Chen, and S.-W. Cheong, Phys. Rev. B **59**, 13573 (1999).
[55] M. v. Zimmermann, C. S. Nelson, J. P. Hill, D. Gibbs, M. Blume, D. Casa, B. Keimer, Y. Murakami, C.-C. Kao, C. Venkataraman, T. Gog, Y. Tomioka, and Y. Tokura, Phys. Rev. B **64**, 195133 (2001).
[56] J. C. Loudon, S. Cox, A. J. Williams, J. P. Attfield, P. B. Littlewood, P. A. Midgley, and N. D. Mathur, Phys. Rev. Lett. **94**, 097202 (2005).